# 水平管群を流下する液膜表面波の生成とガス吸収促進の機構解明

# 2.2 Three-Dimensional Wave Dynamics on a Falling Film and Associated Mass Transfer

*The evolution of solitary waves into three-dimensional (3-D) waves was experimentally observed on a vertically falling water film at mainly Re = 10–100. At Re greater than 40, 2-D solitary waves are very unstable in the face of spanwise perturbations of approximately 2-cm wavelengths and disintegrate into isolated horseshoe-shaped solitary waves and clusters of dimples between the horseshoes, whereas wavefront modulations are limited to low levels at Re below 40. Horseshoes of larger velocities have larger curvature heads, and extend longer oblique legs upward. Curving capillary ripples preceding each horseshoe widen their wavelengths with an increase in the wavefront inclination, showing that the ripples possess the characteristics of the shallow-water capillary waves. The horseshoes may hold vortices inside, and they have similarities in shape and size to hairpin vortices observed in laminar–turbulent transition regions of boundary layers on walls. The disintegration of waves into dimples is caused by a capillary instability similar to the one for breakup of a cylindrical soap film. This transition of wave dynamics at Re ≈ 40 is associated with a drastic change in the mass transfer from the surface into the film.*

## Introduction

Liquid films falling down inclined or vertical walls are frequently encountered in natural and industrial processes. The falling films are unstable and surface waves occur on the films when the Reynolds number *Re* (defined in the subsection on mass transfer coefficient and dimensionless groups) exceeds a critical value. Instabilities of the film flow are convective (Liu et al., 1993; Joo and Davis, 1992a; Cheng and Chang, 1995), and upstream noise perturbations selectively develop into surface waves as they flow downstream (Chang et al., 1996a, b; 2002).

Typical wave evolution when a uniform film is formed on a vertical wall can be seen in Figure 1. Two-dimensional (2-D) deformations become visible on a smooth film surface at some distances from the film inlet, and then rapidly develop into saturated 2-D waves that travel distances of several wavelengths in a quasi-stationary state. During the quasistationary motion, separations between these waves gradually become uneven, associated with increases

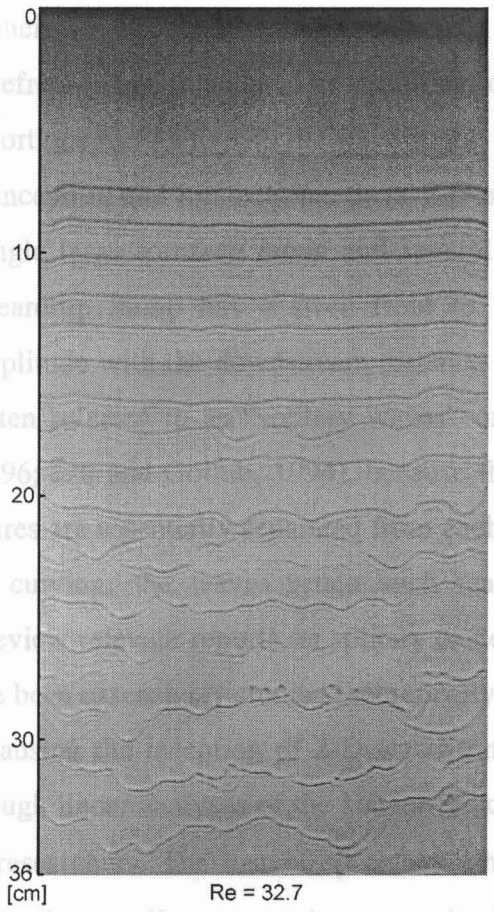


Fig. 1. Shadow image of waves naturally occurring on a falling film at *Re*=32.7 without controlled perturbations imposed on film flow.
Refer to the subsection on surface structures of waves and their shadows, and Figure 2 for the relationship between wave structures and their shadows.

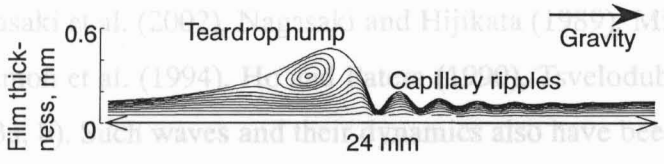


Fig. 2. Teardrop-hump/capillary-ripple structure and vortex in the hump constructed by numerical simulation for a vertically falling water film at *Re*=36.6.
The isoconcentration contours show a vortex in the hump. [A reprint of Figure 5-d by Nagasaki et al (2002).]

in transverse deformation of their wavefronts. Then adjacent waves interact with each other and coalesce to distort the wavefronts significantly. The resulting distorted waves with large separations increase their distortions further to split the wavefronts.

Except for the periods of inception and interactions, these 2-D and 3-D waves have surface structures consisting of a single large *teardrop hump* and several small *capillary ripples*, as shown in Figure 2. Each teardrop hump has a steep front to form capillary ripples that exponentially decrease in amplitude with the downstream distance from the front of the hump. Such wave structures are often referred to as "solitary waves" or "solitary humps" (Chang, 1994; Ramaswamy et al., 1996; Liu and Gollub, 1994), because the humps that dominate the dynamics of the wave structures are essentially separated from each other. Whether wavefronts are horizontal, slanting, or curving, the waves retain such teardrop-hump/capillary-ripple structures. Here we mainly review relevant reports on solitary or nearly solitary waves, though close-packed waves also have been extensively studied theoretically and experimentally.

The primary instability causing the inception of 2-D waves on a smooth film surface has been extensively studied through linear analyses of the Navier-Stokes equations by Yih (1963), Benjamin (1957) and other researchers. The instability occurs when the wave number, $\alpha$, is smaller than a critical value or the cutoff wave number $\alpha_c$, and with increasing wave number the growth rate of the instability increases to the maximum and then decreases to vanish at $\alpha_c$. The wave numbers observed experimentally at the wave inceptions on smooth surfaces scatter to some extent, and are about or are smaller than the theoretical wave number for the maximum growth rate or the *fastest growing* wave number $\alpha_m$ (Pierson and Whitaker, 1977).

The steady traveling 2-D waves were constructed at small *Re* (*Re* $\approx$ 15 or less for vertical water films) and at larger *Re* through nonlinear long-wave evolution equations reduced from the Navier-Stokes equations, by Pumir et al. (1983), Joo et al. (1991), Ooshida (1999) among others, and through the full Navier-Stokes equations or boundary-layer formulas of the Navier-Stokes equations by Nagasaki et al. (2002), Nagasaki and Hijikata (1989), Miyara (2000), Ramaswamy et al. (1996), Salamon et al. (1994), Ho and Patera (1990), Tsvelodub and Trifonov (1992) and Chang et al. (1993a, b). Such waves and their dynamics also have been experimentally captured by Kapitza and Kapitza (1965), Alekseenko et al. (1985, 1994), and Nosoko et al. (1996) by imposing pulses at constant frequencies on the inlet film flow. These techniques of controlling temporal upstream perturbations cause 2-D waves to travel in a quasi- stationary state over distances of about ten or more wavelengths. When compared, the results of these theoretical

and numerical studies showed good agreements with the experimental observations.

The 3-D secondary instability leading to wavefront deformation has been studied through long-wave evolution equations by Joo and Davis (1992a, b), and through the boundary-layer formulas of the Navier-Stokes equations by Trifonov (1991) and Chang et al. (1994). Their constructions of 3-D waves are limited to small Reynolds numbers ($Re \approx 10$ or less). The 3-D instability has a cutoff transverse wave number, and the instability grows when its wave number is smaller than the cutoff value. The instability grows much more slowly than the primary one, and gradually increases transverse distortions on saturated 2-D waves (Chang et al., 1994). The nearly solitary waves hold surface structures similar to the original 2-D wave structures, even after the transverse distortion has developed (Trifonov, 1991; Chang et al., 1994). Recently Chang and Demekhin (2002) performed a preliminary analysis of 3-D waves at small to large *Re* through the generalized Kuramoto- Sivashinsky equation, one of the long-wave evolution equations, and showed that the wave structures holding 2-D cross sections with transversely modulated wavefronts are stable at a certain *Re* range, whereas the wave structures begin to disintegrate into several disconnected 3-D humps at *Re* beyond that range.

Wave structures analogous to the teardrop-hump/ capillary-ripple cross sections, along with their 3-D distributions and time variations, were experimentally observed on films falling down a plane inclined slightly from the horizontal (Liu et al., 1995). It was observed that waves evolve much more slowly on the slightly inclined film than on vertical ones. They showed that when 2-D waves with large constant spacings are excited, transverse modulations of the wavefronts slowly develop and then level off at small transverse amplitudes with about 3-cm transverse wavelengths. When close spaced 2-D waves are excited, the waves coalesce with their neighbors, and eventually teardrop-hump/capillary-ripple structures with rather irregular wavefront modulations become dominant far downstream.

When the waves are restricted to the 2-D, wave coalescence events have been numerically constructed on a long film by Chang et al. (1996a, b; 2002). They showed that solitary humps irreversibly coalesce to form a single large teardrop hump, with associated rapid acceleration and widening of hump separations. The resulting large teardrop humps coalesce several times with front-running smaller teardrop humps in a cascading fashion as they travel downstream.

Mass transfer from the surface into a falling liquid film is strongly dependent on the flow structures in the film, since diffusivities in liquid are very low (Himmelblau, 1964). Surface waves have been found experimentally to cause severalfold increases in the mass-transfer

coefficient in falling films (Emmert and Pigford, 1954; Kamei and Oishi, 1956; Seban and Faghri, 1978). The mass-transfer coefficient increases with *Re* and experimental curves of the coefficient have a break on the log-log scale at *Re* = 40–75 where the slope of the curve sharply decreases (Bakopoulos, 1980; Hikita et al., 1959; Nakoryakov et al., 1983). The break evidently shows that some changes in the dynamics of surface waves occur at the break. Although some have tried to explain such breaks (Nakoryakov et al., 1983; Hikita et al., 1959), the relationship between the mass transfer and the wave dynamics has remained unclear.

Yoshimura et al. (1996) experimentally determined the mass-transfer enhancement caused by 2-D teardrop-hump/capillary-ripple structures on a short vertical water film that was 24 cm high, using the technique of controlling temporal perturbations. With the aid of numerical simulations of 2-D waves by Nagasaki and Hijikata (1989), Yoshimura et al. showed that flow circulation or vortices in the teardrop humps renew the film surface to allow concentration boundary layers to develop along short distances between the teardrop humps, and to be much thinner than the film thickness. The 2-D waves monotonously increase these renewal effects with increasing heights and speeds of the humps. The vortices are so weak that they are visualized with isoconcentration contours in gas-absorbing wave structures, as shown in Figure 2 (Nagasaki et al., 2002) and with streamlines in the coordinates translating with the wave speed (Miyara, 2000). Roberts and Chang (2000) constructed a theoretical model of the mass-transfer enhancement of such vortices in 2-D humps, and explained the experimental observations of a sharp rise in the mass- transfer enhancement with *Re* increasing from 10 to 40. Recently, Vazquez-Una et al. (2000) found a similar mass transfer enhancement by surface waves on films flowing on a horizontal plane, and reported that the mass-transfer coefficient monotonously increases with wave amplitude.

Experimental techniques controlling upstream perturbations have often been successfully used in explorations of transitions of boundary-layer flow on walls or in channels, and in the vortex developments in free shear layers (Nishioka et al., 1981; Acardar and Smith, 1987; Lasheras and Choi, 1988). In this work, we employed similar techniques where time-periodic perturbations of constant frequencies and spanwise perturbations of constant intervals were imposed on the inlet film flow on a vertical plane. When such spatiotemporal perturbations of relatively low frequencies are imposed, 2-D waves evolve into 3-D waves with regular behaviors by skipping complicated wave interactions and coalescence. The resulting wavefront patterns were observed by shadowgraphy. Our efforts were mostly confined to observations of

such waves at $10 < Re < 100$ to capture the possible changes of the wave dynamics at the break of mass transfer coefficient curve.

## Experimental Methods

### *Apparatus and procedure*

We used two experimental apparatuses to observe surface waves on a film falling down a vertical plane and to determine the mass-transfer coefficient of a film falling inside a vertical tube. For the wave observations, tap water is made to flow through a silicone tube from a head tank into a water-holding compartment at the top of the glass plate where water is horizontally distributed along the plate (Figure 3a). Then water is passed through a uniform-width channel between the glass plate and a stainless steel bar to form a film on the plate. Either a short or a long glass plate is used to form a film on a 20.5-cm-wide and 24.5-cm-long area or on a 20.5-cm × 49- cm area of the plate. Controlled spatiotemporal perturbations can be imposed on the film flow by beating the silicone tube with a speaker-driven thin plate at constant frequencies $f$, and by putting fine needles in contact with the film along the inlet at constant spanwise intervals, $\lambda_{z,ndl}$. Two types of spatial perturbations are imposed on the film flow by changing the contact angle of the needle surfaces to water. When the contact angle of water on the needle surface is small, the needles pull up the water surface to locally increase the flow rate which results in *positive* perturbations. Conversely, *negative* perturbations occur when the contact angle is wide and locally decrease the flow rate. Water temperature and volumetric flow rate are measured at the bottom exit of the apparatus using a T-type thermocouple, a flask, electric balance and a stopwatch. A flash from a stroboscope passes horizontally through the film and the glass plate, forming shadows of the waves on a screen right behind the plate. A digital camera synchronized with the stroboscope captures the shadows.

Films falling inside a tube eliminate side-wall effects, which a film on a plane always has. Tap water flows into a two-story compartment, where it is evenly distributed through 17 capillary tubes arranged along the inner wall of the glass tube, which then forms a 95-cm-high film falling inside the glass tube of 9.6 mm inner diameter (Figure 3b). Oxygen gas from a cylinder is fed into the water in a bottle to cause bubbling and then made to flow into the glass tube from its base, leaving the tube from its top. With oxygen gas flowing through the core space of the glass tube, oxygen rich water and its accompanying oxygen bubbles flow from the bottom of the tube into a bubble-separating bottle, after which bubble-free water flows into the

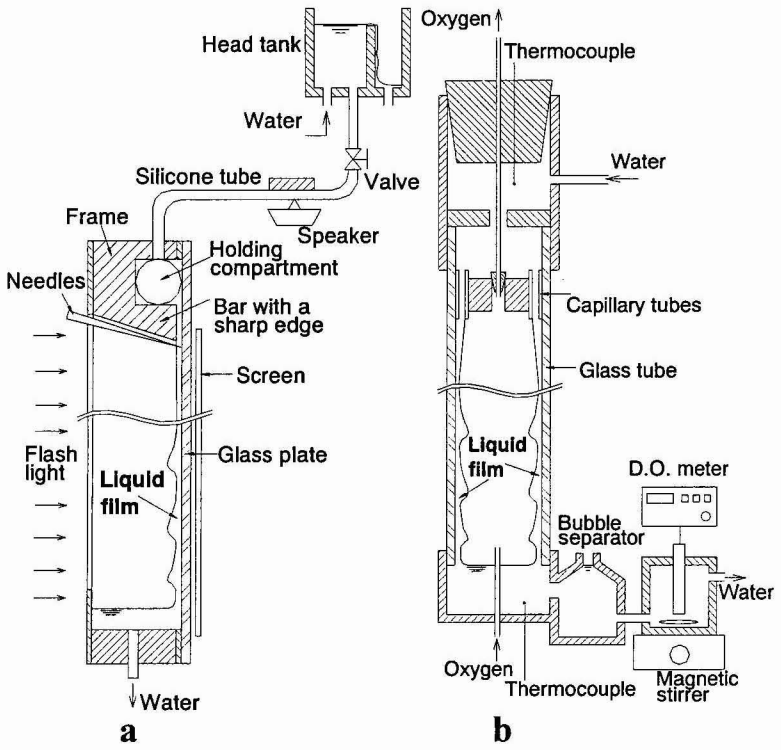


Fig. 3. Experimental apparatuses **a** for a film falling down a vertical plane and **b** for a gas-absorbing film falling inside a vertical tube.

container, where dissolved oxygen concentration $C_{out}$ is measured. Water temperature is measured at the top and the bottom of the tube. The dissolved concentration of oxygen in the water that enters the container directly from the faucet is also measured prior to and immediately after each series of experimental runs. The film temperature, $T$, and the concentration $C_{in}$ at the film inlet are assumed to be averages of these temperature and concentration measurements, respectively. The experiments of mass transfer were performed at a range of $T$ = 15–24 °C and $Re$ = 20–900.

***Mass transfer coefficient and dimensionless groups***

Assuming that the local mass-transfer coefficient is constant along the film, the mean mass-transfer coefficient, $k_L$,, formulated in terms of the logarithmic mean concentration difference, may be given as

$$k_L = \frac{Q}{\pi(d-2\delta)L} \ln \frac{C_s - C_{in}}{C_s - C_{out}} \tag{1}$$

where $Q$, $d$, $\delta$, $L$, and $C_s$ are the volumetric flow rate in the film, the inner diameter of the glass tube, the mean film thickness, the film height, and the saturated concentration of oxygen, respectively. The increase in surface area due to waves is slight (Fulford, 1964), and therefore the surface area of the film is assumed to be $\pi(d-2\delta)L$ within the acceptable range. The mean film thickness $\delta$ for laminar and turbulent flow can be calculated by the correlation for the Nusselt film and by Brauer's (1956) empirical formula, respectively

$$\delta = \left(\frac{3\nu^2 Re}{g}\right)^{1/3} \quad \text{for laminar flow} \tag{2}$$

$$\delta = 0.302\left(\frac{3\nu^2}{g}\right)^{1/3} \mathrm{Re}^{8/15} \quad \text{for turbulent flow} \tag{3}$$

where g and $\nu$ are the gravitational acceleration and the kinematic viscosity of liquid, respectively.

The Reynolds number $Re$, the Sherwood number $Sh$, and the Schmidt number $Sc$ are defined as $Re = \Gamma/\nu$, $Sh = k_L\delta/D$, and $Sc = \nu/D$, respectively, where $\Gamma$ and $D$ are the volumetric flow rate per unit length of wetted perimeter and mass diffusivity, respectively. The physical properties $\nu$, $D$, and $C_s$ are functions of the film temperature $T$. Values for $\nu$ are available from the Data Book (JSME, 1986), and values for $D$ and $C_s$ were derived from the Stokes-Einstein equation

(referred to in Bird et al., 1960), with $D = 2.341\times10^{-9}$ m$^2$/s at $T$ = 25 ℃ (Himmelblau, 1964), and from the correlation by Truesdale et al. (1955), respectively. The saturated vapor pressure of water reduces the partial pressure of oxygen at the film surface and $C_s$, and this reduction is calculated from Henry's law to determine the $C_s$.

***Surface structures of waves and their shadows***

When light rays pass through wave valleys and ridges, the rays diverge and converge onto the screen behind the film, respectively. Hence, a teardrop-hump/capillary -ripple structure forms a set of dark and bright strips on the screen, as shown in all snapshots in this article. The valleys have larger curvatures on bottoms than those on the neighboring ridges (see Figure 2), and therefore darker strips are more noticeable than the bright ones. While the deepest valley in front of the teardrop hump distinctly forms the darkest strip among the set of strips, the valleys of capillary ripples farther from the teardrop hump form less dark strips with decreasing amplitudes. Likewise, higher peak teardrop humps form deeper valleys in front of them, resulting in darker strips on the screen. These distinctive dark strips of the deepest valleys may represent the wavefronts of teardrop humps. As a result, the shadows of waves may show transverse variations of wavefronts; separations between teardrop humps, $\lambda_{hmp}$; the number of capillary ripples preceding each teardrop hump; the wavelengths of the capillary ripples; qualitatively the peak heights of the teardrop humps and the amplitudes of the capillary ripples.

## Results and Discussion

***Mass transfer enhancement by surface waves***

A measured variation of the Sherwood number *Sh* with the Reynolds number *Re* is compared in Figure 4 with the empirical correlations by Bakopoulos (1980) and with a solution to the equation of diffusion into a smooth surface film of a semiparabolic velocity profile by Tamir and Taitel (1971). Bakopoulos constructed the correlations to fit the data measured with vertical long water films (mostly film heights of 1 m or higher) by Emmert and Pigford (1954), Kamei and Oishi (1956), Hikita et al. (1959), and Lamourelle and Sandall (1972). Tamir and Taitel's solution changes the relationship between *Sh* and *Sc* with the ratio of film height to film thickness, and here an average value of the present measurements, *Sc* = 479, was employed to draw the curve of the solution in Figure 4 for comparison.

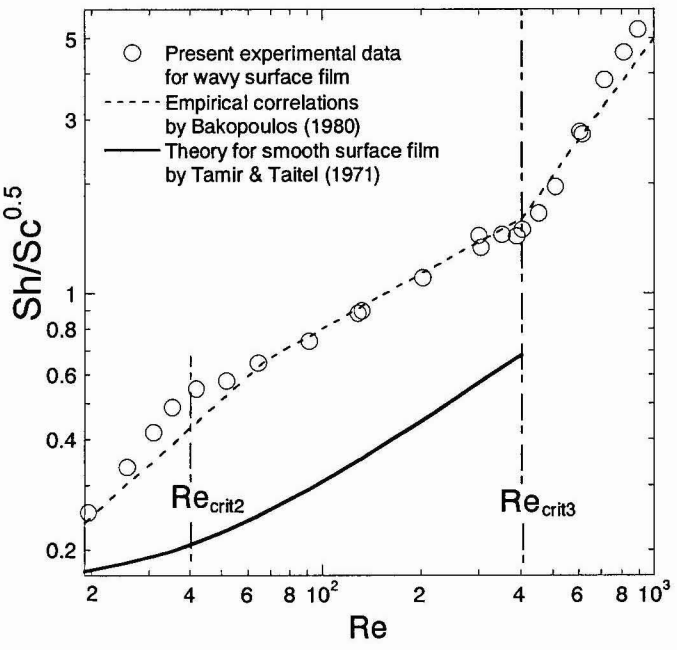


Fig. 4. Mass transfer enhancement by surface waves and two breaks of mass transfer curve.

The experimental data show that the increase in $Sh$ is rapid in $Re \lesssim 40$, gentle in $40 \lesssim Re \lesssim 400$, and then rapid in $Re \gtrsim 400$, showing two breaks at $Re \approx 40$ and 400. The slopes of the data are approximately 1.0, 0.5, and 1.4 in $Re \lesssim 40$, $40 \lesssim Re \lesssim 400$ and $Re \gtrsim 400$, respectively. Since the mean film thickness $\delta$ increases with $Re$, as described by Eqs. 2 and 3, the mass-transfer coefficient $k_L$ is in proportion to $Re^{2/3}$, $Re^{1/6}$, and $Re^{4/5}$ in $Re \lesssim 40$, $40 \lesssim Re \lesssim 400$, and $Re \gtrsim 400$, respectively, showing very weak dependence of $k_L$ on $Re$ in $40 \lesssim Re \lesssim 400$. The present data are in good agreement with the correlations by Bakopoulos in $Re \gtrsim 75$, but are a little larger in $Re \lesssim 75$. The experimental data, which he collected for the correlations, scatter to some extent, and the present measurements fall within the scattering.

A break occurs at $Re \approx 400$ on both the present data and the correlations by Bakopoulos, and it may represent a transition from wavy laminar flow to turbulent flow. Brauer (1956), Feind (1960), and Emmert and Pigford (1954) determined that the transition occurs at $Re \approx 400$, based on their measurements of variations of film thickness, wall shear stress, and mass-transfer coefficient with $Re$, respectively. The present measurements are in good agreement with their findings.

Another break occurs at $Re \approx 40$ and 75 on the present data and on the correlations by Bakopoulos, respectively. Likewise, Emmert and Pigford (1954), Hikita et al. (1959), and Nakoryakov et al. (1983) reported such breaks in $40 \lesssim Re \lesssim 75$. Jackson (1955) proposed the "turbulent wave" concept, where turbulence is localized within peak regions of solitary waves, which travel downstream on a laminar substrate film. Hikita et al. tried to explain the break of the mass-transfer curve with the aid of the turbulent-wave concept. Recent numerical simulations have denied such localized turbulence at low $Re$ (Nagasaki et al., 2002; Miyara, 2000).

Comparison of the present $Sh$ data with the solution by Tamir and Taitel (1971) shows that surface waves rapidly increase the mass-transfer coefficient, $k_L$, with $Re$ up to 2.6 times the solution at $Re$ = 40, associated with large differences in the slope, and then gently increase $k_L$ with a small slope to 2.2 times the solution at $Re$ = 400. Emmert and Pigford (1954), Kamei and Oishi (1956), Hikita et al. (1959), Seban and Faghri (1978), and Nakoryakov et al. (1983) also reported similar increases in mass-transfer coefficients caused by surface waves.

Figure 5 shows the shadows of the waves on a water film falling inside the vertical tube. As flashlight rays pass horizontally through the vertical circular tube, the shadows of waves on two narrow areas of the film are enlarged due to the curvature of the tube wall and projected

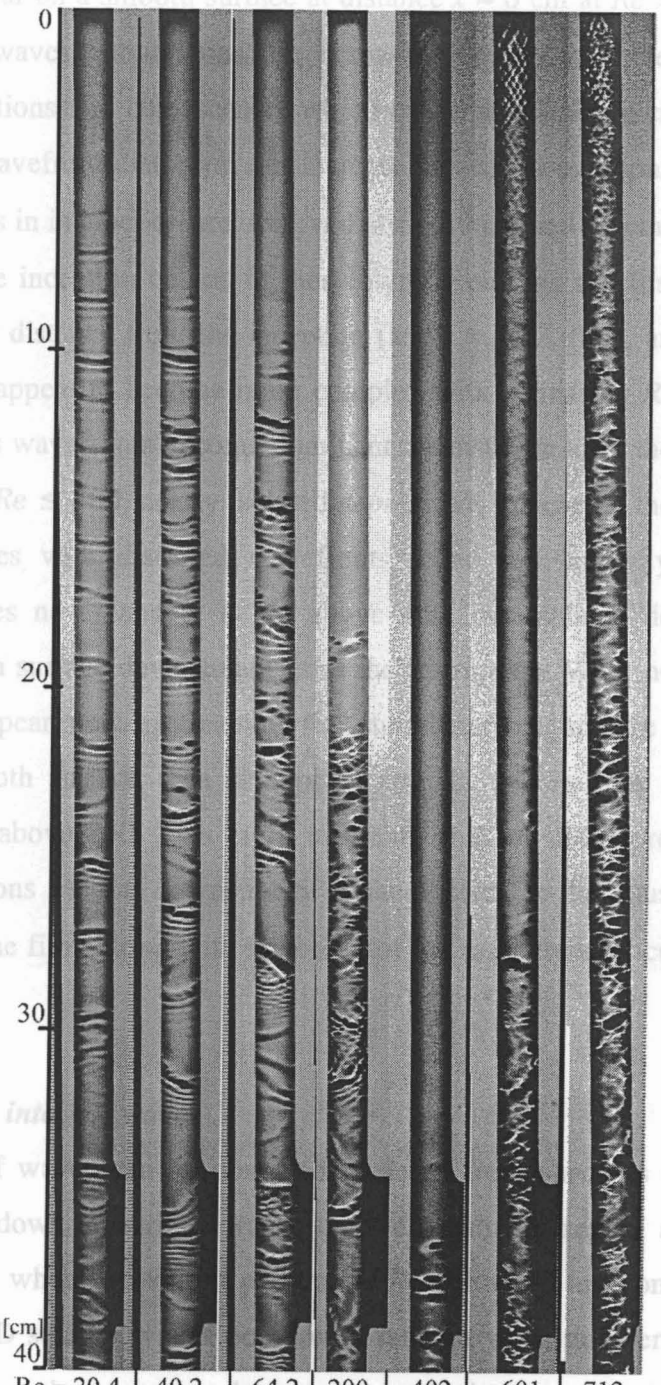


Fig. 5. Shadow images of waves on films falling inside a glass tube.
The images capture the films at $x$=0–40 cm.

together on the screen. Because these shadows cause some difficulties in observing the wave dynamics, we provide a brief overview of the wave dynamics in this section.

2-D waves appear on a smooth surface at distance $x \approx 6$ cm at $Re = 20.4$ from the film inlet (Figure 5). These waves then demonstrate increasing distortions of their wavefronts, associated with wave interactions and coalescence, which cause drastically increasing wave separations and much more wavefront distortion (an increase in wave separation due to such coalescence and adjacent waves in interaction are observed at $x \approx 19$ cm and 30 cm at $Re = 20.4$ in Figure 5). At larger *Re*, wave inception occurs further downstream, and the first wave interaction event occurs at a shorter distance from the inception (at $Re = 40.2$, 64.2, and 200 in Figure 5). The wave interactions appear to become more complex with increasing *Re*, and highly 3-D waves holding continuous wavefronts become dominant downstream after the wave interactions at $Re \lesssim 200$. At $200 \lesssim Re \lesssim 400$, nearly isolated *depressions* appear on the smooth surface (Figure 5), and 3-D waves with distorted wavefronts seem to eventually become dominant far downstream. Waves never appear at *Re* above 400, but isolated depressions are dominant throughout the film surface downstream from their inception. With increasing *Re*, from 400 to 700 depressions appear more upstream on the smooth surface, and the smooth surface becomes rougher. The smooth surface area disappears and the whole film surface is covered with depressions at *Re* above 700. This rapid upstream shift of the depression inception and the dominant depressions on the downstream surfaces seem to be caused by the transition to turbulent flow in the film, along with the break of the mass transfer curve at $Re \approx 400$ (Figure 4).

***Evolution of waves into 3-D waves***

The dynamics of waves can be observed in detail from shadows of films falling down a vertical plane. Shadows of surface waves on a downstream region after their inception are shown in Figure 6, where wavefront patterns at *Re* below 40 are compared with those at *Re* above 40. Since 2-D solitary waves occur with random wave numbers and random velocities around the fastest growing wave number, $\alpha_m$, and velocity, respectively, they gradually change separations between them, growing transverse modulations of their wavefronts, after which interactions of adjacent waves occur at some distance from their inception (a typical wave interaction is seen between the third and the fourth waves from the top in Figure 6b). When two solitary waves come close, they either almost merge along their wavefronts, or they rapidly

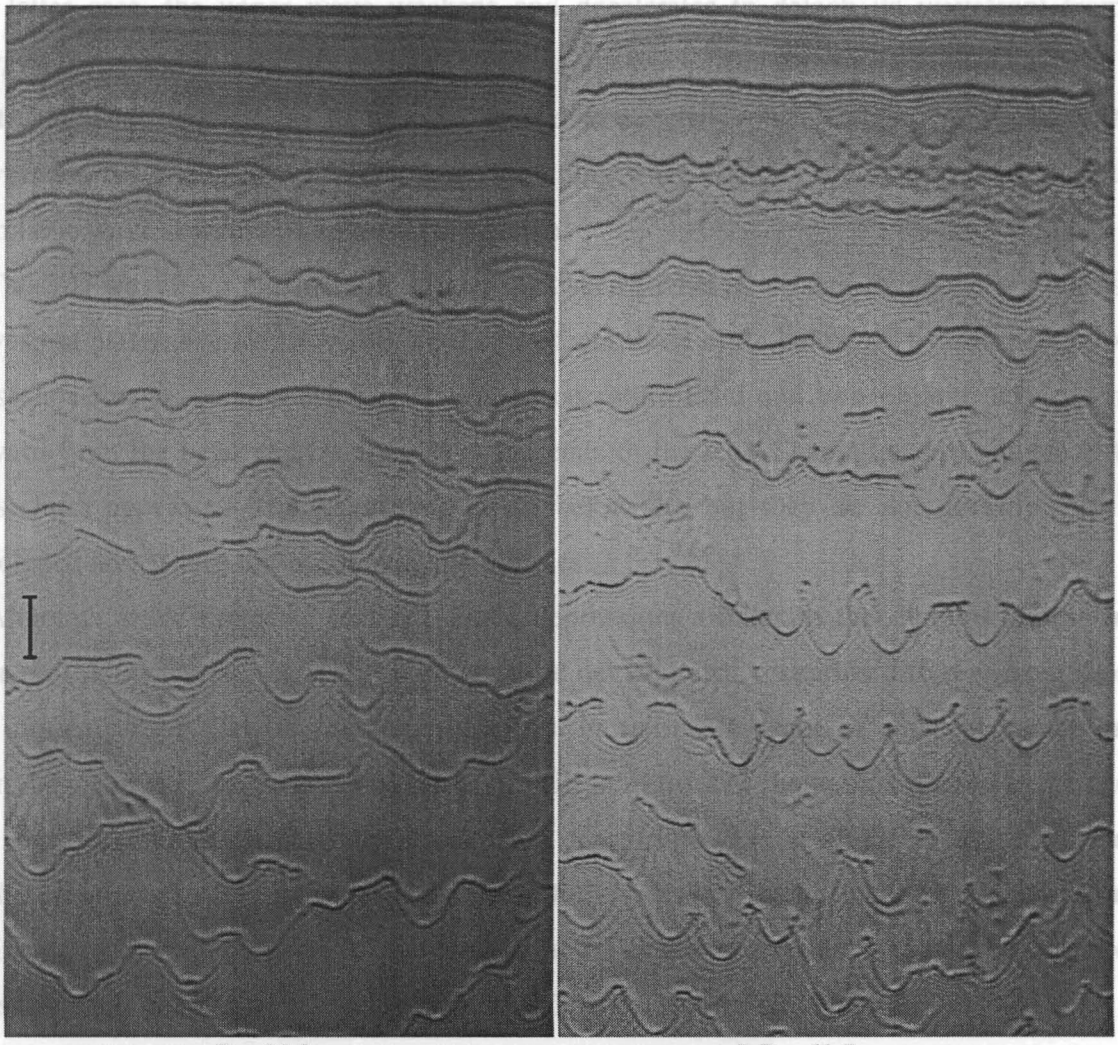

**a** Re=30.3 **b** Re=61.7

Fig. 6. Shadow images of waves without controlled perturbations imposed on film flow. The images capture the films at $x$=14–48 cm, and the bar is 2 cm long.

increase the transverse modulations of their wavefronts and partially merge at several points. In the latter case, the upper wave weakens and decelerates to detach its wavefront from the merging parts and to leave its partner (see the sixth wave from the top in Figure 6a). The next upstream wave catches up to absorb these disconnected waves, which greatly distorts its wavefront. After such wave interactions, including wave coalescence, 3-D wavefront patterns with large wave separations appear downstream.

The 3-D wavefront patterns are different between *Re* below 40 and *Re* above 40, that is, the wavefront patterns at *Re* above 40 are distinct from those at *Re* below 40 by a large number of horseshoe-shapes, each consisting of a large curvature head and two oblique legs extending upward from the head and by dimples at the ends of the legs. Several shapes similar to those horseshoes appear on the wavefronts at *Re* below 40, but they do not develop into fully developed horseshoes nor accompanying dimples.

Although at *Re* under 40 isolated single depressions similar to the dimples appear in the course of the wave interactions, they may have development scenarios different from those of the dimples at the ends of the horseshoe legs. Partial coalescence of adjacent humps causes sharp bends in the wavefronts, and the deep valleys in front of the humps deepen at the ends of the sharp bends and disintegrate into isolated depressions. Liu et al. (1995) observed similar birth scenarios of such depressions on films falling down a plane inclined slightly from the horizontal. The birth scenarios of the dimples at the ends of horseshoe legs will be described in the subsection on the structure of horseshoe and partial wave disintegration.

When the controlled spatiotemporal perturbations are imposed on the inlet film flow at constant low frequencies and at constant spanwise intervals, solitary 2-D waves develop into 3-D waves with regular behaviors (Figure 7), skipping the complex interactions of waves. These waves may demonstrate the differences of the wave dynamics between *Re* below 40 and above 40. At $Re \approx 20$, solitary waves are unstable to 3-D perturbations of spanwise intervals of $\lambda_{z,ndl} \approx 3$ cm or larger. Wavefronts gradually increase their modulation amplitudes of transverse wavelengths $\lambda_z \approx 3$ cm or larger, and then saturate the modulations to have nearly sinusoidal shapes, that is, the shapes of the wavefronts are asymmetrical with upward curvatures smaller than downward curvatures (Figure 7b). The waves are not unstable to the perturbations of $\lambda_{z,ndl} \approx 1$ cm or smaller. When transverse perturbations of $\lambda_{z,ndl} \approx 1$ cm or smaller are imposed, the waves decrease the perturbations but gradually increase the amplitudes of transverse modulations of $\lambda_z \approx 3$ cm and larger wavelengths (Figure 7a). The cutoff transverse wavelength

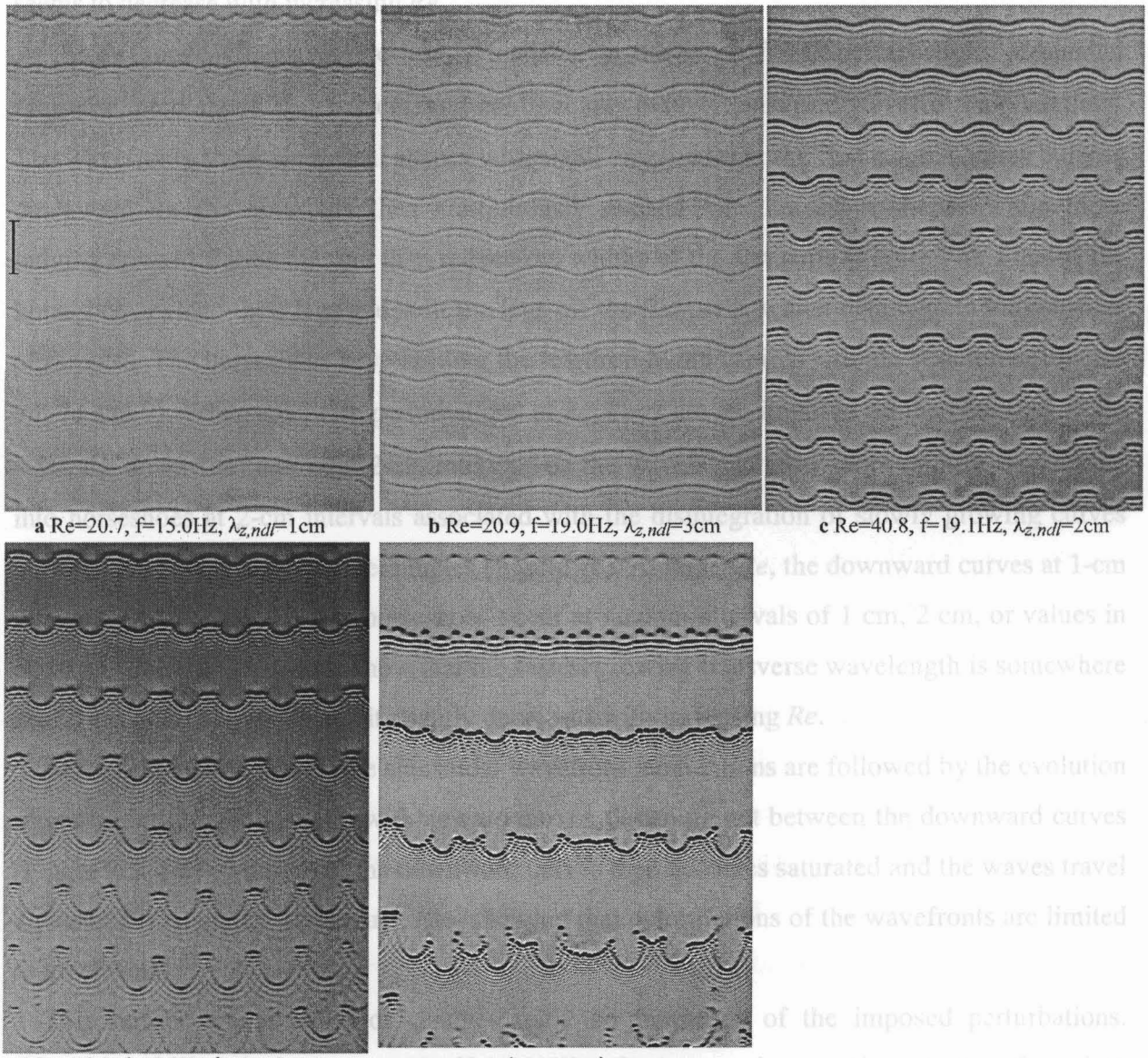

**a** Re=20.7, f=15.0Hz, $\lambda_{z,ndl}$=1cm **b** Re=20.9, f=19.0Hz, $\lambda_{z,ndl}$=3cm **c** Re=40.8, f=19.1Hz, $\lambda_{z,ndl}$=2cm

**d** Re=59.3, f=17.0Hz, $\lambda_{z,ndl}$=2cm **e** Re=88.6, f=15.1Hz, $\lambda_{z,ndl}$=1cm

Fig. 7. Shadow images of waves excited with controlled spatio-temporal perturbations of constant frequencies $f$ and constant spanwise intervals $\lambda_{z,ndl}$. The spatial perturbations are positive.